Geosci. Instrum. Method. Data Syst. Discuss., 3, 251–303, 2013
www.geosci-instrum-method-data-syst-discuss.net/3/251/2013/
doi:10.5194/gid-3-251-2013

Geoscientific Instrumentation Methods and Data Systems Discussions
Open Access

A sensitivity study for far infrared balloon-borne limb emission sounding of stratospheric trace gases

J. Xu, F. Schreier, P. Vogt, A. Doicu, and T. Trautmann

DLR – German Aerospace Center, Remote Sensing Technology Institute, Oberpfaffenhofen, 82234 Weßling, Germany

Received: 29 January 2013 – Accepted: 1 May 2013 – Published: 14 May 2013

Correspondence to: J. Xu (jian.xu@dlr.de)

Published by Copernicus Publications on behalf of the European Geosciences Union.

Abstract

This paper presents a sensitivity study performed for trace gases retrieval from synthetic observations by TELIS (TErahertz and submillimeter LImb Sounder) which is a stratospheric balloon-borne cryogenic heterodyne spectrometer. Issues pertaining to hydroxyl radical (OH) retrieval from the far infrared measurements by the 1.8 THz channel are addressed. The study is conducted by a retrieval code PILS (Profile Inversion for Limb Sounding) developed to solve the nonlinear inverse problems arising in the analysis of infrared/microwave limb sounding measurements. PILS combines a line-by-line forward model with automatic differentiation for computing Jacobians and employs regularized nonlinear least squares inversion. We examine the application of direct and iterative regularization methods and evaluate the performance of single- and multi-profile retrievals. Sensitivities to expected errors in calibration procedure, instrumental knowledge and atmospheric profiles have been analyzed. Nonlinearity effect, inaccurate sideband ratio, and pointing error turned out to be the dominant error sources. Furthermore, the capability of multi-channel simultaneous retrieval from the far infrared and submillimeter data has been investigated. The errors and averaging kernels infer that the quality of the obtained hydrogen chloride (HCl) can be improved by significantly better exploitation of information from the observations.

1 Introduction

Far infrared and submillimeter limb sounding is a well-established technique for atmospheric remote sensing because numerous trace gases have features in this spectral range. Furthermore, emission observations are independent of sunlight and hence can contribute to the understanding of the diurnal cycles of chemical processes. In addition, aerosols and ice clouds have negligible effect, which also makes the far infrared and submillimeter observations advantageous. The latest spaceborne missions comprise SMR (Sub-Millimetre Radiometer) (Murtagh et al., 2002) on the Odin

GID
3, 251–303, 2013

satellite launched in 2001, MLS (Microwave Limb Sounder) (Waters et al., 2006) in 1991 and 2004 aboard the UARS and Aura satellites, respectively, and SMILES (Superconducting subMIllimeter-wave Limb-Emission Sounder) (Kikuchi et al., 2010) from October 2009 to April 2010. In particular, Aura/MLS has the ability to measure thermal emission from the far infrared (Terahertz) spectral range.

TELIS (TErahertz and submillimeter LImb Sounder) is a new balloon-borne cryogenic heterodyne spectrometer designed to investigate the vertical distribution of stratospheric trace gas species associated with ozone depletion and climate change. The instrument utilizes state-of-the-art superconducting heterodyne technology and allows limb sounding of the Earth's atmosphere with high spectral resolution and long flight duration. TELIS was mounted on a stratospheric balloon gondola together with the MIPAS-B (Michelson Interferometer for Passive Atmospheric Sounding - Balloon) instrument (Friedl-Vallon et al., 2004), developed by the Karlsruhe Institute of Technology (KIT), and mini-DOAS (Differential Optical Absorption Spectrometer) operated by the University of Heidelberg. From a flight altitude of 30–40 km, TELIS scans the stratosphere and upper troposphere with 1.5–2 km altitude sampling. The combination of TELIS and MIPAS-B yields a wide range of the electromagnetic spectrum for atmospheric research and offers great synergies for cross-validation of measured chemical constituents. In addition, TELIS serves as a technology demonstrator to future space-borne limb sounders. The instrument has participated in three scientific campaigns in Kiruna, Sweden from March 2009 to March 2011.

TELIS was developed by a consortium of European institutes that include the German Aerospace Center (DLR), the Netherlands Institute for Space Research (SRON), and the Rutherford Appleton Laboratory (RAL) in the United Kingdom. The ambitious spectral coverage of the TELIS instrument is accomplished by use of three frequency channels: a highly compact 500 GHz channel, a 480–650 GHz channel (de Lange et al., 2010) based on the Superconducting Integrated Receiver (SIR) technology, and a tunable 1.8 THz channel (Suttiwong et al., 2009) with enhanced stability provided by RAL, SRON, and DLR, respectively. The incoming atmospheric radiation is transmitted from

GID
3, 251–303, 2013

a dual offset Cassegrain telescope through the front-end transfer optics where the signals are separated and coupled into each dedicated channel (Suttiwong, 2010).

The 1.8 THz channel measures the signal at a local oscillator (LO) frequency f_{LO} between 1790 and 1880 GHz. The measured spectrum is then generated from the two sidebands with respect to the LO frequency since the TELIS instrument operates in double sideband (DSB) mode. In case of the 1.8 THz channel the spectrum is recorded in the intermediate frequency f_{IF} domain ranging from approximately 4 to 6 GHz (2 GHz spectral bandwidth). The signal is split into four 500 MHz autocorrelator segments. Thus, the measured spectrum covers the frequency domains at $f_{LO} - f_{IF}$ and $f_{LO} + f_{IF}$. For the 480–650 GHz channel f_{IF} ranges from 5 to 7 GHz.

The primary scientific goal of the TELIS/MIPAS-B/mini-DOAS flight has been to measure the time-dependent chemistry of chlorine (Cl) and bromine (Br), and to achieve the closure of chemical families (NO_y, Cl_y, Br_y, HO_x) inside the polar vortex. Regarding the TELIS instrument, the main target of the 1.8 THz channel is the hydroxyl radical (OH). Further stratospheric species HO_2, HCl, HOCl, O_3, O_2, CO, NO, NO_2, and H_2O including its isotopologues can also be measured in the frequency range of 1790–1880 GHz. OH is a key reactive species for photochemical reactions that regulate ozone throughout most of the stratosphere and mesosphere. The demand and interest of having the capability to measure the OH radical in the atmosphere has been consequently increasing.

OH possesses pairs of triplets in the far infrared spectral region, such as 61 cm^{-1} (1.8 THz), 83 cm^{-1} (2.5 THz), 101 cm^{-1} (3.0 THz), 118 cm^{-1} (3.5 THz). Carli et al. (1989) and Carlotti et al. (2001) observed the 3.5 THz feature with a balloon-borne far infrared Fourier Transform spectrometer. Pickett and Peterson (1993) used a balloon-borne two-channel (101 and 118 cm^{-1}) Fabry-Perot instrument "FILOS" to retrieve stratospheric OH, and middle to upper stratospheric OH concentrations were estimated from thermal emission far infrared (83–230 cm^{-1}) observations with the balloon-borne "FIRS" Fourier transform spectrometer (Jucks et al., 1998). In August 1997, the airborne heterodyne spectrometer THOMAS performed OH observations between about

GID
3, 251–303, 2013

30 and 90 km over a full diurnal cycle (Englert et al., 2000). The characterization of OH diurnal variability in the stratosphere and mesosphere has also been analyzed using measurements from the Aura/MLS instrument (Minschwaner et al., 2011). Both instruments observe OH at 2.5 THz, whereas TELIS selected 1.8 THz for monitoring OH in the lower and middle stratosphere. Although the OH emission at 1.8 THz is weaker than that at 2.5 THz, the former one was chosen for the sake of higher sensitivity of the HEB (Hot Electron Bolometer) mixer at 1.8 THz and risks associated with the development of the 2.5 THz solid state local oscillator (Mair et al., 2004).

For being able to analyze the TELIS (or further spaceborne, e.g. SMILES, Odin/SMR) measurements and retrieve trace gas profiles, the Remote Sensing Technology Institute at DLR has developed a retrieval code PILS (Profile Inversion for Limb Sounding) dedicated to high resolution infrared/microwave radiative transfer calculation and reliable inversion scheme. In this paper, we present the physical and mathematical basics of PILS as well as its capability of trace gas retrievals from synthetic TELIS measurements. Particular emphasis is placed on the capability study of the 1.8 THz channel. For a study of the 480–650 GHz channel we refer to de Lange et al. (2009). The forward model used to simulate the measurements and the inversion methodology with diagnostics are described in Sect. 2. In Sect. 3 we firstly discuss the performance of OH vertical profile retrieval from a single limb scan with perfect instrumental knowledge. A sensitivity analysis is then conducted to estimate the impact of uncertainties in calibration procedure, the atmospheric and instrument parameters in the forward model. Section 4 identifies the capability of multi-channel simultaneous processing by implementing HCl retrieval. A summary and an outlook to future work and products are given in Sect. 5.

GID
3, 251–303, 2013

2 Forward model and inversion methodology

2.1 Radiative transfer and instrument modelling

In atmospheric remote sensing, the radiation seen by a sensor is described by the theory of radiative transfer with an appropriate instrument model, accounting for spectral response, field-of-view, and – in case of heterodyne – the sideband ratio. Neglecting scattering and assuming local thermodynamical equilibrium, the intensity (radiance) I at wavenumber ν at position s along the line-of-sight is given by the integral form of the Schwarzschild equation (Liou, 2002; Zdunkowski et al., 2007)

$$I(\nu,s) \;=\; I(\nu,s_0)\,\mathrm{e}^{-\tau(\nu;s_0,s)} \;+\; \int_{s_0}^{s} \mathrm{d}s'\; B(\nu,T(s'))\,\mathrm{e}^{-\tau(\nu;s',s)}\,\alpha(\nu,s')\;, \tag{1}$$

where $I(\nu,s_0)$ is the source radiation at position s_0, and $B(\nu,T)$ represents the Planck function at temperature T. The optical depth τ is defined as the path integral of the volume absorption coefficient $\alpha(\nu,s)$ which is essentially the product of molecular cross section k and number density summed over the molecule. For high resolution a line-by-line evaluation is considered, i.e. k is computed by summing over the contributions from many lines: $k(\nu;p,T) = \sum_{\mathrm{l}} S_{\mathrm{l}}(T)\; g(\nu;\hat{\nu}_{\mathrm{l}},\gamma_{\mathrm{l}}(p,T))$, where each line is characterized by its position $\hat{\nu}_{\mathrm{l}}$, the temperature-dependent line strength $S(T)$, and a Voigt line shape function g (with half width γ) describing the combined effect of pressure (p) broadening and Doppler broadening.

The subsequent step is to model the instrument performance as precisely as possible. For the 1.8 THz channel, the monochromatic spectrum is convolved with an instrumental line shape function yielded by Fourier transform of a Hamming apodization function. For the 480–650 GHz channel, a Lorentzian line shape function defined by the frequency locking (de Lange et al., 2009) is used. Moreover, a superposition of pencil-beam spectra can be done by convolving with an angle-dependent field-of-view function which is Gaussian shaped with a vertical full width half maximum (FWHM) of

GID
3, 251–303, 2013

0.1043 deg (6.3 arcmin) in the 1.8 THz channel (Suttiwong, 2010). The field-of-view at 619.1 GHz is a Gaussian curve with a FWHM of 0.1805 deg (10.8 arcmin).

For TELIS measurements, the measured spectrum is the weighted superposition of the spectra of the two sidebands by the sideband ratio. Ideally the sideband ratio r is equal to one, that is to say, both sidebands offer equal gain response. In Sect. 3.3.2 the effect of deviations in the sideband ratio from unity on retrieval results will be addressed.

2.2 Inversion scheme and regularization

The discretization of the radiative transfer equation leads to the nonlinear data model $\boldsymbol{y}^{\delta} = \boldsymbol{F}(\boldsymbol{x}) + \boldsymbol{\delta}$, where the mapping $\boldsymbol{F} : \mathbb{R}^n \rightarrow \mathbb{R}^m$ represents the forward model, $\boldsymbol{x} \in \mathbb{R}^n$ is the state vector, $\boldsymbol{y}^{\delta} \in \mathbb{R}^m$ is the noisy data vector, and $\boldsymbol{\delta} \in \mathbb{R}^m$ is the measurement error. The state vector comprises the atmospheric parameters to be retrieved, while the data vector is a concatenation of all limb spectra (Carlotti, 1988). Our analysis considers a semi–stochastic data model in the sense that the true solution $\boldsymbol{x}_{\mathrm{t}}$ is deterministic, but the measurement error $\boldsymbol{\delta}$ is stochastic with zero mean and the noise covariance matrix $\mathbf{S}_{\delta} = \mathcal{E}\left\{\boldsymbol{\delta} \cdot \boldsymbol{\delta}^T\right\} = \sigma^2 \mathbf{I}_m$, where $\mathcal{E}$ is the expected value operator, σ^2 is the noise variance, and $\mathbf{I}_m$ is the identity matrix in $\mathbb{R}^m$.

The inverse problem is ill-posed and a regularization method shall be used in order to obtain a solution with physical meaning. Tikhonov regularization (Tikhonov, 1963) is a direct regularization method, in which the regularized solution $\boldsymbol{x}_{\lambda}$ minimizes the objective function

$$\mathcal{F}(\boldsymbol{x}) = \|\boldsymbol{F}(\boldsymbol{x}) - \boldsymbol{y}^{\delta}\|^2 + \lambda \|\mathbf{L}(\boldsymbol{x} - \boldsymbol{x}_{\mathrm{a}})\|^2 \tag{2}$$

$$= \left\| \begin{array}{c} \boldsymbol{F}(\boldsymbol{x}) - \boldsymbol{y}^{\delta} \\ \sqrt{\lambda}\mathbf{L}(\boldsymbol{x} - \boldsymbol{x}_{\mathrm{a}}) \end{array} \right\|^2, \tag{3}$$

where $\mathbf{L}$, λ, and $\boldsymbol{x}_{\mathrm{a}}$ represent the regularization matrix, the regularization parameter, and the a priori state vector, respectively. The regularization matrix, which encapsulates

GID
3, 251–303, 2013

our a priori knowledge about the solution, is chosen as the Cholesky factor of an a priori profile covariance matrix $\mathbf{S}_x$, corresponding to an exponential correlation function, i.e. $\mathbf{S}_x^{-1} = \mathbf{L}^T\mathbf{L}$, where

$$[\mathbf{S}_x]_{ij} = [\boldsymbol{x}_a]_i [\boldsymbol{x}_a]_j \exp\left(-2\frac{|z_i - z_j|}{l_i + l_j}\right) \quad (4)$$

with $i, j = 1, \ldots, n$, and the lengths l_i determine the correlation between the atmospheric parameters at different altitudes z_i. Note that for an equidistant altitude grid and $l_i = l$ for all $i = 1, \ldots, n$, we have $\mathbf{L} \to \mathbf{I}_n$ as $l \to 0$, and $\mathbf{L} \to \mathbf{L}_1$ as $l \to \infty$, where $\mathbf{L}_1$ is the discrete approximation to the first-order derivative operator. The proper selection of the regularization parameter λ is critical, since the regularized solution should reflect a trade off between the residual $\|\boldsymbol{F}(\boldsymbol{x}) - \boldsymbol{y}^\delta\|^2$ and the penalty term $\|\mathbf{L}(\boldsymbol{x} - \boldsymbol{x}_a)\|^2$. In this study, a priori parameter choice methods (Doicu et al., 2010) are applied to determine the regularization parameter.

Another widely-used so-called optimal estimation method (Rodgers, 2000) can be regarded as a stochastic version of Tikhonov regularization, in which the regularization parameter is incorporated into the a priori profile covariance matrix, that is, $\mathbf{S}_x^{-1} = \lambda\mathbf{L}^T\mathbf{L}$. In this case, a trade off between the measurement and the a priori profile requires a proper selection of $\mathbf{S}_x$. Furthermore, the optimal estimation method is more sensitive to the choice of a priori profile than Tikhonov regularization. In view of those target species lacking a priori knowledge, the retrieval with Tikhonov regularization can be less influenced by the inadequate a priori information.

Numerical experience shows that the Tikhonov function in Eq. (2) usually has many local minima and a descent method for solving the optimization problem tends to get stuck especially for severely ill-posed problems. In this case, iterative regularization methods are an attractive alternative: the number of iteration steps plays the role of the regularization parameters, and the iterative process is stopped after an appropriate number of steps in order to avoid an uncontrolled amplification of the noise error. An intercomparison between Tikhonov regularization and two iterative methods will

GID
3, 251–303, 2013

be given in Sect. 3.2. In the iteratively regularized Gauss–Newton method (Bakushinskii, 1992), the regularization parameters are the terms of a geometric sequence, i.e. $\lambda_k = q\lambda_{k-1}$, for some $q < 1$, and the stopping index is chosen according to the discrepancy principle in dependence of the noise level and the noisy data vector. The regularizing Levenberg–Marquardt method also uses a decreasing sequence of regularization parameters, but the penalty term depends on the previous iterate instead of the a priori.

Frequently the inversion deals with the joint retrieval of several concentration profiles corresponding to different molecules, and solves the underlying multi-component problem by means of regularization. If the vector $\boldsymbol{x}_p$ comprises the concentration profile of the pth molecule, then the state vector $\boldsymbol{x}$ is a concatenation of all $\boldsymbol{x}_p$. Assuming that the components of the state vector are independent, all individual regularization matrices $\mathbf{L}_p$ are assembled into a global regularization matrix $\mathbf{L}$ with a block-diagonal structure:

$$\mathbf{L} = \begin{bmatrix} \sqrt{\lambda_1}\mathbf{L}_1 & 0 & \cdots & 0 \\ 0 & \sqrt{\lambda_2}\mathbf{L}_2 & \cdots & 0 \\ \vdots & \vdots & \ddots & \vdots \\ 0 & 0 & \cdots & \sqrt{\lambda_N}\mathbf{L}_N \end{bmatrix}, \tag{5}$$

where N is the number of gas components. Multi-parameter regularization methods can be classified according to the goal of the inversion process. The regularization parameters λ_k are determined by minimizing certain objective functions corresponding to the entire state vector or to the main component of the state vector, respectively (Doicu et al., 2010).

2.3 Inversion diagnostics

A sensitivity analysis reveals our expectation on the inversion process. The sensitivity of the forward model with respect to components of the state vector is described in terms of the Jacobian matrix $\mathbf{K} = \partial \boldsymbol{F}/\partial \boldsymbol{x}$. More precisely, for a change in the kth

GID
3, 251–303, 2013

component of the state vector about the a priori, $\Delta \boldsymbol{x}_k = \boldsymbol{x} - \boldsymbol{x}_\mathrm{a}$, with $[\Delta \boldsymbol{x}_k]_j = \varepsilon \left[\boldsymbol{x}_\mathrm{a}\right]_k$ for $j = k$, and $[\Delta \boldsymbol{x}_k]_j = 0$ for $j \neq k$, the change in the forward model is given componentwise by $[\Delta \boldsymbol{F}_k]_i = \varepsilon \left[\mathbf{K}(\boldsymbol{x}_\mathrm{a})\right]_{ik} \left[\boldsymbol{x}_\mathrm{a}\right]_k$ with $i = 1, \ldots, m$. In this context, one can say that the instrument is sensitive over the "entire" spectral domain to a $\pm\varepsilon$-variation in the kth component of the state vector about the a priori, if $|[\Delta \boldsymbol{F}_k]_i| > \sigma$ for all $i = 1, \ldots, m$.

The quality of the regularized solution can be assessed through an error analysis. By defining the regularized generalized inverse (also known as the gain matrix) $\mathbf{K}^\dagger = \left(\mathbf{K}^T\mathbf{K} + \lambda \mathbf{L}^T\mathbf{L}\right)^{-1}\mathbf{K}^T$ and neglecting the higher-order terms of the solution, the retrieval error can be expressed as

$$\boldsymbol{e}_\lambda \;=\; \boldsymbol{x}_\lambda - \boldsymbol{x}_\mathrm{t} \;=\; \boldsymbol{e}_\mathrm{s} + \boldsymbol{e}_\mathrm{y} + \boldsymbol{e}_\mathrm{b}\,, \tag{6}$$

where $\boldsymbol{e}_\mathrm{s} = (\mathbf{A} - \mathbf{I}_n)(\boldsymbol{x}_\mathrm{t} - \boldsymbol{x}_\mathrm{a})$ is the smoothing error that quantifies the loss of information due to the regularization, $\boldsymbol{e}_\mathrm{y} = \mathbf{K}^\dagger\boldsymbol{\delta}$ is the noise error that quantifies the loss of information due to the measurement noise $\boldsymbol{\delta}$, and $\boldsymbol{e}_\mathrm{b} = \mathbf{K}^\dagger\boldsymbol{\delta}_\mathrm{b}$ is the model parameter error. Here, $\mathbf{A} = \mathbf{K}^\dagger\mathbf{K}$ is the averaging kernel matrix and $\boldsymbol{\delta}_\mathrm{b}$ is the forward model error. The smoothing error is not a computable quantity, but it can be estimated by $\boldsymbol{e}_\mathrm{s} \approx (\mathbf{A} - \mathbf{I}_n)(\boldsymbol{x}_\lambda - \boldsymbol{x}_\mathrm{a})$. In a semi-stochastic setting, the smoothing and the model parameter errors are likely to be deterministic, while the noise error is stochastic with zero mean and covariance matrix. The model parameter error is caused by an inaccurate knowledge of the atmospheric and instrument parameters $\boldsymbol{b}$ employed in the forward model. If $\Delta\boldsymbol{b}$ comprises the uncertainties in $\boldsymbol{b}$, then the forward model error can be computed as

$$\boldsymbol{\delta}_\mathrm{b} \;=\; \mathbf{K}_\mathrm{b}\Delta\boldsymbol{b} \;\approx\; \boldsymbol{F}(\boldsymbol{x}_\mathrm{t}, \boldsymbol{b} + \Delta\boldsymbol{b}) - \boldsymbol{F}(\boldsymbol{x}_\mathrm{t}, \boldsymbol{b}) \tag{7}$$

with $\mathbf{K}_\mathrm{b}$ being the Jacobian matrix with respect to $\boldsymbol{b}$. The quality of the regularized solution is estimated through the mean square error matrix defined by

$$\mathbf{S}_\lambda \;=\; \mathcal{E}\left\{(\boldsymbol{x}_\lambda - \boldsymbol{x}_\mathrm{t})(\boldsymbol{x}_\lambda - \boldsymbol{x}_\mathrm{t})^T\right\} \;\approx\; \mathbf{S}_\mathrm{s} + \mathbf{S}_\mathrm{y} + \mathbf{S}_\mathrm{b} \tag{8}$$

GID
3, 251–303, 2013

with $\mathbf{S}_s = \boldsymbol{e}_s \boldsymbol{e}_s^T$, $\mathbf{S}_y = \sigma^2 \mathbf{K}^\dagger \mathbf{K}^{\dagger T}$, and $\mathbf{S}_b = \boldsymbol{e}_b \boldsymbol{e}_b^T$.

2.4 Implementation

The forward model of PILS is one of the variants of GARLIC (Generic Atmospheric Radiation Line-by-line Infrared Code), a modern Fortran reimplementation of MIRART (Modular InfraRed Atmospheric Radiative Transfer) (Schreier and Schimpf, 2001; Schreier and Böttger, 2003). GARLIC/MIRART is designed for arbitrary observation geometry (limb, nadir, up-looking) and instrumental line shape and field-of-view. For optimized line-by-line computations a combination of rational approximations for the Voigt line shape (Schreier, 2011) and a multigrid approach (Schreier, 2006) is implemented. MIRART has been verified in extensive intercomparisons (e.g. von Clarmann et al., 2002; Melsheimer et al., 2005). Besides, Hedelt et al. (2011) used MIRART to model observations of the Venus transit in 2004. Mendrok et al. (2007) and Vasquez et al. (2013) have introduced multiple/single scattering to estimate cirrus cloud parameters from MIPAS data and to model SCIAMACHY's Venus observations, respectively.

Efficient yet accurate computation of the Jacobian **K** is crucial for the solution of (constrained) nonlinear least squares problems. Although derivatives are straightforward to evaluate, a manual implementation is tedious and error prone; on the other hand, finite differences are extremely time consuming and unreliable because the appropriate perturbation is difficult to estimate. Surprisingly automatic or algorithmic differentiation (AD) (Griewank, 2000) is rarely used in atmospheric remote sensing although a variety of tools (for Fortran, C/C++, etc.) have been developed in the past decades, see http://www.autodiff.org/. Schreier and Schimpf (2001); Schreier and Böttger (2003) used ADIFOR (Bischof et al., 1998) to implement derivatives in the Fortran 77 MIRART code utilizing source-code transformation and Ungermann (Ungermann et al., 2011) introduced derivative code in JURASSIC2 (Jülich Rapid Spectral Simulation Code Version 2) by overloading in C++ employing DCO/C++. PILS utilizes the source-to-source AD tool TAPENADE (Hascoët and Pascual, 2013) (version 3.4) to generate derivatives

GID
3, 251–303, 2013

in forward (tangent) mode, and the total computation time for all spectra comprising an entire limb sequence of 10 tangent altitudes plus Jacobians for 23 altitude levels is increased by just a factor of 2 in contrast to the pure forward calculation. For a discussion of the pros and cons of the various AD techniques see, e.g. Bischof and Bücker (2000).

The evaluation of the augmented vector in Eq. (3) relies on the use of optimization solver in the PORT Mathematical Subroutine Library (Fox et al., 1978, available at http://www.netlib.org/port/). The solver uses a trust-region method in conjunction with a Gauss–Newton model and a quasi-Newton model (Dennis Jr. et al., 1981). After convergence, PILS delivers the diagnostic quantities introduced in Sect. 2.3, including the relative difference with respect to the true profile and the retrieval error (the square root of the diagonal elements of the mean square error matrix $\mathbf{S}_\lambda$).

3 OH retrieval from the 1.8 THz channel

3.1 Retrieval setup

In order to explore the inversion performance and potential error sources, a set of numerical simulations has been made. We retrieve OH from a single limb-scanning sequence that largely resembles typical TELIS observations of the 1.8 THz channel. The limb tangent altitude varies from 15 to 33 km in steps of 2 km, and the observing altitude is set to 35 km (the dotted maroon horizontal line in the figures). The major instrument and geometry parameters used for simulating the synthetic spectra are listed in Table 1.

H_2O, O_3, HCl, HOCl, and HO_2 have been included in the simulation as the interfering molecules. The line parameters were read from the HITRAN 2008 (Rothman et al., 2009) spectroscopic database, and the semi-empirical Clough–Kneizys–Davis (CKD) (Clough et al., 1989) model was used to account for the H_2O continuum. It is important to choose a proper spectral microwindow covering targeted OH lines with

GID
3, 251–303, 2013

minimum overlapped contributions from other atmospheric spectral lines. Here the LO frequency is set to 1830.10 GHz ($\approx 61.04\,\mathrm{cm}^{-1}$) with an intermediate frequency range of 4–6 GHz, as employed during the campaigns in 2009 and 2011. The atmospheric pressure, temperature and molecular concentration profiles were taken from the AFGL subarctic winter reference model (Anderson et al., 1986). The retrieval was performed on an altitude grid with a step of 2 km between 15 and 25 km, a step of 2.5 between 25 and 50 km, and a step of 5 km between 50 and 85 km. Typical spectra are depicted in Fig. 1 for this OH microwindow.

The Jacobian matrices with respect to the molecular concentrations for a tangent altitude of 25 km are plotted in Fig. 2 (the derivatives above 45 km are not shown here). In the derivative spectra of OH, two triplet pairs are visible at both sides of the intermediate frequency point of about 4.65 GHz. It should be noticed that the strong triplet occurs in the upper sideband while the weaker one lies in the lower sideband. Both peaks are found to be larger than the middle trough with a factor of 1.5 and the peaks are about two to five orders of magnitude larger than those of the other molecules.

A sequence of noise contaminated spectra is essential for realistic inversion analysis. In the present simulations only the radiometric noise was considered. The signal-to-noise ratio (SNR) for a single spectrum can be estimated by

$$\mathrm{SNR} = \frac{T_{\mathrm{sig}}}{T_{\mathrm{sys}}} \sqrt{\Delta f\, t}\,, \tag{9}$$

where the TELIS spectral resolution Δf is 2.16 MHz, and the integration time t is 1.5 s. For the 1.8 THz channel the average system noise temperature ranges between 3000 and 4000 K (Birk et al., 2010). In case of the selected OH microwindow, the system noise temperature T_{sys} can reach 3800 K. According to Fig. 1, the equivalent brightness temperatures of the OH emission line T_{sig} are above 75 K, which causes the lowest signal-to-noise ratio of SNR $\approx$ 35. The worst-case scenario was used to conduct the retrieval feasibility study. The noise δ, which is added to the noise-free spectrum for

GID
3, 251–303, 2013

each tangent altitude, is described by a Gaussian distribution. There is no correlation in terms of the added noise over the frequency range.

3.2 Retrieval results

In this subsection, temperature, pressure, HCl, HOCl, HO_2 were assumed to be known and set to their a priori values. Perfect atmospheric and instrument parameters were assumed in the forward model so that $\boldsymbol{e}_b = 0$. The initial guess and a priori profile of the target molecule(s) $\boldsymbol{x}_0$ and $\boldsymbol{x}_a$, respectively, were assumed to be identical and chosen as

$$\boldsymbol{x}_0 = \boldsymbol{x}_a = \begin{cases} 0.1\ \boldsymbol{x}_t & \text{if } z < 30\,\text{km}\ , \\ 0.12\ \boldsymbol{x}_t & \text{if } z \geq 30\,\text{km}\ . \end{cases} \tag{10}$$

A sensitivity study involving the variations of the limb radiances $\Delta \boldsymbol{F}_k^s$, corresponding to the sth tangent height and to a 10 % variation of the concentration profile of relevant molecules in the kth level is illustrated in Fig. 3. The results show that information about the concentration profile in a specific level is mainly given by the spectra corresponding to the tangent heights below the altitude level (see also Fig. 2). The instrument is sensitive to OH in the frequency range of 4.5–5 GHz. In this spectral range and for altitude levels above 27.5 km, the sensitivity of OH is superior to that of other molecules. Below 27.5 km, the OH concentration is rather low and of no significant importance for the measured radiance signal. In this regard, it can be expected that the retrieval of OH at altitude levels below 27.5 km is essentially based on the a priori information and not from the measurement. For the OH retrieval problem, the variations of the spectra at 27.5 and 30 km are not substantially larger than the noise level, that can imply a worse noise error below 30 km.

GID
3, 251–303, 2013

3.2.1 One-profile retrieval

First of all, we consider only OH as target molecule (with accurate a priori knowledge of O_3 and H_2O) to clarify the retrieval capability of the selected microwindow. The estimation of an appropriate regularization parameter plays an important role in finding a reliable retrieval solution. For this purpose, we solve the one-profile retrieval problem for various regularization parameters λ, and for each λ the relative solution errors $\epsilon(\lambda) = \|\boldsymbol{x}_\lambda - \boldsymbol{x}_t\|/\|\boldsymbol{x}_t\|$ are computed. In Fig. 4a we illustrate the relative solution errors of OH volume mixing ratio (VMR) for Tikhonov regularization, the iteratively regularized Gauss–Newton method, and the regularizing Levenberg–Marquardt method. For iterative methods, λ is the initial value of the regularization parameter, while at all subsequent iteration steps, the regularization parameters are the terms of a geometric sequence with the ratio $q = 0.8$. The error curve corresponding to Tikhonov regularization possesses a minimum, and by convention, the minimizers of the solution errors represent the optimal values of the regularization parameter.

Still the iteratively regularized Gauss–Newton method yields reliable results for large initial values of the regularization parameter. Evidently, a stronger regularization at the beginning of the iterative process requires a larger number of iterations as can be seen in Fig. 4b. The regularizing Levenberg–Marquardt method is also insensitive to overestimations of the regularization parameter. However, the results in Fig. 4 illustrate that the regularizing Levenberg–Marquardt method is inferior to the iteratively regularized Gauss–Newton method: for large initial values of the regularization parameter, the solution errors are larger. Henceforth, we choose Tikhonov regularization essentially for efficiency reasons as it converges quickly (with ≤ 5 iteration steps) disregarding any choice of λ.

For $\lambda = 1 \times 10^{-4}$, the retrieved OH concentration profile along with the corresponding quantity in terms of relative difference is plotted in Fig. 5a. The relative difference is up to 12 % (at 15 km) in the plotted altitude range. The quality of the retrieval is also assessed by the retrieval error encapsulating the combined effect of the noise and the

GID
3, 251–303, 2013

smoothing errors (Fig. 5b). The smoothing error dominates the retrieval error budget from 15 to 27.5 km where the noise error is fairly small, which implies that the retrieval error at these altitudes relies on the a priori information and the vertical resolution is poor. The noise error as the main error stretches from 27.5 km upward, while the smoothing error appears to take less effect.

3.2.2 Two-profile retrieval

For the two-profile retrieval we consider a joint retrieval of OH and O_3. For multi-profile retrieval a smaller spectral window of 500 MHz, corresponding to the second autocorrelator segment of 4.5–5 GHz, is used. Based on the previous sensitivity analysis, the sensitivity of OH is highest in this spectral range. In Fig. 1 a pair of strong O_3 lines appears in the wings of the OH triplet, which implies that an uncertainty in the concentration profile of O_3 may have a distinct influence on the retrieval results of OH. To investigate how well OH can be retrieved without an accurate a priori knowledge of ozone, O_3 is retrieved simultaneously with OH.

For the joint retrieval of OH and O_3 we minimize (2) in conjunction with Eq. (5) for a set of regularization parameters $\boldsymbol{\lambda} = \left(\lambda_{\mathrm{OH}}, \lambda_{\mathrm{O_3}}\right)$, and then compute the solution errors in each component, that is, $\epsilon_{\mathrm{OH}}(\boldsymbol{\lambda}) = \|\boldsymbol{x}_{\mathrm{OH},\lambda} - \boldsymbol{x}_{\mathrm{OH,t}}\|/\|\boldsymbol{x}_{\mathrm{OH,t}}\|$ and $\epsilon_{\mathrm{O_3}}(\boldsymbol{\lambda}) = \|\boldsymbol{x}_{\mathrm{O_3},\lambda} - \boldsymbol{x}_{\mathrm{O_3,t}}\|/\|\boldsymbol{x}_{\mathrm{O_3,t}}\|$, as well as the total solution error $\epsilon(\boldsymbol{\lambda}) = \sqrt{\epsilon_{\mathrm{OH}}(\boldsymbol{\lambda})^2 + \epsilon_{\mathrm{O_3}}(\boldsymbol{\lambda})^2}$. The results in Fig. 6 show that for $\lambda_{\mathrm{OH}} = 1 \times 10^{-4}$ and $\lambda_{\mathrm{O_3}}$ ranging between 1×10^{-6} and 1, the total solution error is small and almost constant. However, in order to obtain smaller residual after convergence, the regularization parameters of OH and O_3 are set to $\lambda_{\mathrm{OH}} = 1 \times 10^{-4}$ and $\lambda_{\mathrm{O_3}} = 1 \times 10^{-6}$, respectively.

The relative differences of OH and O_3 are displayed in the left panel (a) of Fig. 7. Although O_3 is weakly regularized during the retrieval, an error of less than 5 % is found below the observing altitude, however, an underestimate above 35 km can be observed. Concerning OH, errors of less than 15 % with respect to the true profile in

GID
3, 251–303, 2013

both combinations are observed over the whole altitude range, that are comparable to the result of the one-profile fit. The right panel (b) of Fig. 7 illustrates the retrieval error, the smoothing and the noise errors for the retrieved molecules. The retrieval error is dominated by the smoothing error at lower altitudes and by the noise error above 25 km. It is apparent that the vertical resolution of the retrieval of OH is poorer than the O_3 retrieval. The smoothing error of O_3 is very small, which reveals that the main information comes from the measurement itself rather than from the a priori information.

3.2.3 Three-profile retrieval

Another aspect to consider is the three-profile retrieval. The state vector comprises three molecules, i.e. OH, O_3, and H_2O. The same spectral window as the two-profile retrieval is used. The regularization parameters $\lambda_{OH} = 1 \times 10^{-4}$, $\lambda_{O_3} = 2 \times 10^{-6}$, and $\lambda_{H_2O} = 5 \times 10^{-6}$ have been chosen by using the technique described in Sect. 3.2.2.

The difference with respect to the true profile in Fig. 8a shows that the OH retrieval can be done over the whole altitude range, although the errors are slightly larger than for the single- and two-profile retrievals. It may suggest that the inaccurate a priori knowledge of H_2O and O_3 could influence the OH retrieval. The retrieval error of OH in Fig. 8b is quite similar to the results above.

Using synthetic noisy measurements based on the perfect instrumental knowledge, the vertical concentration profile of OH can be retrieved in both single- and multi-profile retrieval frameworks in decent quality. A priori knowledge affects the retrieval error and yields a poor vertical resolution at lower altitudes, while the noise error dominates the retrieval error budget at higher altitudes. Although the spectral information over the instrument is limited, the profile of OH above 35 km can still be retrieved due to its high sensitivity in the middle stratosphere. Nonetheless, the imperfect instrumental knowledge and inaccurate atmospheric parameters can degrade the quality of retrieved solution.

GID
3, 251–303, 2013

3.3 Sensitivity to expected error sources

In the retrieval results displayed above, several assumptions of forward model profiles and instrument parameters have been made. However, it is of importance to see how imperfect atmospheric state profiles and instrumental knowledge influence the performance of the retrieval. For this reason, an error analysis has been carried out for atmospheric profiles and instrument parameters. In this study only the most important error sources (known from previous studies, e.g. de Lange et al., 2009, 2012; Baron et al., 2011; Urban et al., 2005) have been considered. As O_3 appears to be important in this OH microwindow, OH and O_3 were considered as the target molecules of multi-profile fitting involved in the following simulations. The selected regularization parameters are $\lambda_{OH} = 1 \times 10^{-4}$ and $\lambda_{O_3} = 1 \times 10^{-6}$. In contrast to Sect. 3.2, the initial and a priori profiles of the target molecules were scaled with a factor of 0.1, or rather, a priori error of 90 %. H_2O, HCl, HOCl, and HO_2 were assumed to be known. In this study we concentrate on the performance of the OH retrieval affected by errors in calibration procedure, instrumental knowledge and atmospheric profiles.

3.3.1 Calibration error

Radiometric accuracy is crucial for a good quality of atmospheric profiles retrieval, especially systematic radiometric errors can result in a bias in the retrieval. For TELIS, a linear radiometric calibration approach is employed. An on-board blackbody unit is used as a hot signal reference and the signal from pointing into deep space is used as a cold signal reference. To reduce drift effects, both blackbodies are measured in short time intervals (ca. every 30 s) between the limb scans. From these hot and cold calibration measurements, the unknowns of the instrument's response function, the radiometric gain and the offset, can be determined and thus allow for a linear radiometric calibration of the measured spectra. However, in the TELIS IF-signal chain nonlinearities are present, which can not be compensated by the linear calibration approach and further lead to systematic errors in radiometric calibrated spectra. To study the

GID
3, 251–303, 2013

influence of the nonlinearity on the retrieval, the linear calibration procedure together with a nonlinear instrument response needs to be modelled.

Assuming a linear response system, the instrument output y^i for a given input signal I_m^i can be given by

$$y^i = G\left(I_m^i + I_{T_{sys}}\right), \qquad \text{with} \quad i = \text{atm, H, C}, \tag{11}$$

where I_m^i denotes a noise-free model spectrum with the index i indicating an atmospheric (atm) spectrum, a hot load (H) spectrum or a cold load (C) spectrum. The offset $I_{T_{sys}}$ represents the modelled intensity of a blackbody at the system noise temperature of the heterodyne receiver and G specifies the radiometric gain. In the linear calibration scheme, the unknowns of the instrument's response, the gain and the offset are then derived from calibration measurements of both known reference blackbodies with

$$G = \frac{y^H - y^C}{I_m^H - I_m^C} \tag{12}$$

and

$$I_{T_{sys}} = \frac{I_m^H y^C - I_m^C y^H}{y^H - y^C}. \tag{13}$$

I_m^H and I_m^C are computed via Planck's law from given brightness temperatures of the hot and cold blackbodies. Consequently, the radiometric calibrated atmospheric spectrum I_{cal}^{atm} can be calculated from the instrument output y^{atm} using Eqs. (12) and (13):

$$I_{cal}^{atm} = \frac{y^{atm}}{G} - I_{T_{sys}}. \tag{14}$$

GID
3, 251–303, 2013

However, according to on-ground characterizations of TELIS using gas cell measurements, the input-output relation of the instrument is nonlinear and therefore Eq. (11) does not hold. Although experiments show a complex combination of nonlinear elements in the IF-signal chain, a more generic approach is employed in this study. The nonlinearities of the instrument can be approximated by an effective, quadratic nonlinearity, which is only sensitive to the integral power along the bandwidth W at the input. As a result, Eq. (11) shall be reformulated as

$$y_{\mathrm{nl}}^{i} = \left(I_{\mathrm{m}}^{i} + I_{T_{\mathrm{sys}}}\right)\left(1 + C_{\mathrm{nl}}\int_{W}\mathrm{d}\nu\,\left(I_{\mathrm{m}}^{i} + I_{T_{\mathrm{sys}}}\right)\right), \tag{15}$$

where C_{nl} is the coefficient which defines the quadratic nonlinearity. For the sake of simplicity, the linear coefficient is set to one. As the nonlinearity is caused by saturation effects in the amplifier chain, $C_{\mathrm{nl}} < 0$ applies. This leads to a compression ω of the output with respect to the linear case with $\omega = 1 - y_{\mathrm{nl}}^{i}/y^{i} < 1$. To calculate the nonlinear outputs y_{nl}^{i}, the quadratic coefficient C_{nl} is chosen such that the compression of the modelled hot load measurement $y_{\mathrm{nl}}^{\mathrm{H}}$ is comparable to the values deduced from laboratory measurements. The nonlinearity is then propagated into the calibration procedure by replacing y^{i} with y_{nl}^{i} in Eqs. (12)–(14).

The obtained calibrated spectra $I_{\mathrm{cal}}^{\mathrm{atm}}$, which are distorted by the nonlinearity, are compared with the pure atmospheric model spectra $I_{\mathrm{m}}^{\mathrm{atm}}$ and then used as input for the retrieval. In case of the OH microwindow, the blackbodies having the temperature of 278 and 2.725 K are used as the hot and cold load, respectively. The compression in the hot load is estimated with $\omega = 20 \pm 10\,\%$. The modelled calibrated spectra at one tangent altitude are plotted in Fig. 9 and compressions of 10 and 30 % are assumed for the nonlinearity. As can be seen from the residuals, the nonlinearity results in a line scaling effect in the calibrated spectra with respect to the ideal case.

Furthermore, the calibrated spectra with the compression of 30 % were used as the worst-case scenario and the retrieval was performed with the noisy synthetic

GID
3, 251–303, 2013

measurements distorted by the nonlinearity. It is expected that the retrieved profile of OH and O_3 can be distorted resulting from the line scaling effect in the measurements. Thus, a pseudo-correction scheme for simulating the linear calibration procedure is implemented in the retrieval, which superimposes the nonlinearity onto the model spectra by Eq. (14) at every iteration step with the given compression quantities ω. The nonlinear outputs y_{nl}^{i} are evaluated by Eq. (15). The radiometric gain G and the offset $I_{T_{\mathrm{sys}}}$ in the nonlinear system are computed by Eqs. (12) and (13), respectively. To access the error propagation onto the retrieval products, an additional 5 % uncertainty was assumed, i.e. the retrievals were repeated with the compression ω set to 25 and 35 %, respectively. The retrieval results of OH and O_3 are compared to the results without the correction in Fig. 10. In this case, neither the noise errors nor the smoothing errors are increased in an evident way. Accordingly, the influence on the retrieval error is low (not shown). The errors in terms of relative difference imply that the nonlinearity effect is more severe on O_3, that causes largest error of 20 % at 15 km. The retrieved OH profile is not affected by the nonlinearity below 21 km due to the fact that there is no strong OH signal below this altitude (see also Fig. 1). The results for correction with 25 and 35 % compression are almost symmetric with respect to the case of 30 % (above 25 km for OH). As expected, the nonlinearity can affect the retrieval of OH at higher altitudes where the spectral feature is strong.

The nonlinearity effect has been studied with the modelled calibration procedure and the corresponding retrieval results from these measurements. The errors with respect to the true profile declare that the nonlinearity can bring about an error on the OH retrieval in the middle stratosphere where the OH lines are easily identifiable. With the pseudo-correction scheme applied to the retrieval, the errors with respect to the true profile are reduced by up to 7 %, as can be inferred from Fig. 10.

3.3.2 Instrumental knowledge: sideband ratio

Uncertainties in the parameters used by the instrument module of the forward model might cause systematic biases in the retrieved vertical profiles. Excluding the

GID
3, 251–303, 2013

calibration error, the most important instrumental error sources for the TELIS observations are discussed below and in Sect. 3.3.3.

The precise knowledge of the receiver sideband ratio is a fundamental requirement for the calculation of the TELIS spectra. An error in the sideband ratio r can result in a systematic change in the contributions of the spectra, and further, an unexpected error in the retrieval results. We define the distorted sideband ratio as $\tilde{r} = r(1+\eta)$ by introducing a relative bias η, the measured spectrum I is expressed as:

$$
\begin{aligned}
I &= \frac{r}{r+1} I_{\mathrm{USB}} + \frac{1}{r+1} I_{\mathrm{LSB}} \\
&= \frac{r}{r+1}\left(1 + \frac{\eta}{r(1+\eta)+1}\right) I_{\mathrm{USB}} + \frac{1}{r+1}\left(1 - \frac{r\,\eta}{r(1+\eta)+1}\right) I_{\mathrm{LSB}} \,, \qquad (16)
\end{aligned}
$$

where I_{USB} and I_{LSB} denote the spectra of the upper sideband (USB) and lower sideband (LSB), respectively. The strong OH line lies in the upper sideband of the selected LO frequency in this study. A positive η means an overestimated contribution of the upper sideband in the spectra, while a negative η will lead to an underestimated intensity. To study the impact of the error in the sideband ratio, the relative bias η has been studied in the following simulation. According to recent laboratory measurements performed for characterization of the sideband ratio, r is estimated to lie in the range of 0.95 to 1.05 for the 1.8 THz channel, i.e. maximal uncertainty of 5 % with respect to the ideal sideband ratio $r = 1.0$. The values ±0.01, ±0.03, ±0.05, and ±0.1 (extreme case) for η are taken into account. The propagated error on the retrieval has been evaluated by using the linear mapping ($\boldsymbol{e}_{\mathrm{b}} = \mathbf{K}^{\dagger}\boldsymbol{\delta}_{\mathrm{b}}$ with Eq. (7)) which relates changes in the solution to changes in the spectra via $\mathbf{K}^{\dagger}$.

For all altitudes below the observing altitude of 35 km, the bias η ($-0.1 \sim 0.1$) in the sideband ratio produces the propagated error of less than 3 % in the retrieved O_3 profile (these results are not shown here). The propagated errors in the OH retrieval are depicted in Fig. 11. The relative retrieval error and the noise error are also included for comparison. The errors introduced by the small biases (0.01 and 0.03) can reach 5–15 % at 21 km and decrease with increasing altitude. The results are found to be

GID
3, 251–303, 2013

more severely influenced by larger biases (0.05 and 0.1). For more clarity, the large sideband ratio bias can result in significant error on the retrieval quality of OH.

In Fig. 12 the errors in terms of relative difference are obtained by retrievals with different η in the sideband ratio. The measurement is for the assumed sideband ratio $r = 1.0$. O_3 is not plotted for the reason that no significant error on the retrieved profile is induced by the sideband ratio bias. In our case, the intensity is sensitive to the contribution of OH in the upper sideband. As judged from Eq. (16) and Fig. 11, the retrieved OH profile is overestimated with positive biases on the sideband ratio, whereas underestimated with negative ones.

3.3.3 Instrumental knowledge: pointing

A pointing error can be characterized by systematic pointing bias and random pointing offset. The pointing error can be expressed by an altitude error at the tangent point, or by an error in the zenith angle of the line-of-sight. The MIPAS-B instrument on the gondola is equipped with a highly stable attitude and heading reference system (Friedl-Vallon et al., 2004). Although TELIS also receives its pointing information from this system, the stability of the connection between both instruments remains to be examined, a fact which could have an impact on the quality of the trace gas retrieval. It has been probed that the systematic pointing bias is 3.4 arcmin on the zenith angle for the 1.8 THz channel, corresponding to a 500 m deviation for the lowest tangent altitude (15 km) in this case.

Assuming that the uncertainty in this systematic pointing bias is up to 1 arcmin, the expected error propagation onto the retrieved profile of OH is plotted in Fig. 13. As this bias is deterministic, the propagated error is estimated by using Eq. (7) in the framework of a linearized forward model about the true state. A propagated error of up to 0.01 ppbv with the uncertainty of 1 arcmin is found below the observing altitude. As a result of very low concentration at lower altitude, the largest propagated error occurs between 15–25 km.

GID
3, 251–303, 2013

The relative differences in the OH profile for a single-target retrieval by assuming the uncertainties of 0.5 and 1 arcmin in the systematic pointing bias (3.4 arcmin) are shown in Fig. 14a. These results are in agreement with the relative propagated errors in Fig. 13b, leading to the conclusion that the forward model is not too nonlinear. The pointing error yields a shift of all gas profiles. As O_3 is the most important contributor to the measurement signal, an unresolved shift of the O_3 profile is the reason for the large relative differences in the OH profile. The relative differences in the OH profile become considerably smaller if a joint retrieval of OH and O_3 is performed, as can be seen in Fig. 14b.

The standard approach for far infrared and microwave limb sounding is to extract the pointing information from measurements of oxygen emission lines. Alternatively, the pointing error can be retrieved for each spectrum in the limb sequence together with the target molecules. In this case the random pointing offset is nearly compensated.

3.3.4 Atmospheric profiles

The accuracy of the temperature profile is vital to the reliability of target gas retrievals. For more precise retrieval results from actual TELIS data, the MIPAS-B temperature retrieval can be a pleasant candidate due to the fact that MIPAS-B and TELIS are both carried by the same gondola frame.

We have assumed an uncertainty of 1 K on the temperature profile for altitudes up to 45 km to investigate the corresponding effect on the retrieval. In Fig. 15, the estimated error propagation onto the retrieved OH profile via Eq. (7) is depicted. Below 27.5 km, the propagated error ranges 10–14 %. The profile is saturated and depleted by up to 0.0006 ppbv respectively with errors of 1 and −1 K in the temperature profile. Between 27.5 and 35 km, a propagated error of up to 7 % is found despite an increased absolute propagated error because of up to two orders of magnitude higher concentration in the stratosphere. It implies that a slight deviation in the temperature profile may cause an error especially at lower altitudes (upper troposphere and lower stratosphere) where the concentration of OH is relatively low.

GID
3, 251–303, 2013

Moreover, we have assessed the propagation of a pressure error onto the OH retrieval by introducing errors of −1 and 1 % for the whole altitude grid. Compared to the error propagation by the temperature profile, the assumed errors on the pressure profile lead to considerable effects between 15 and 30 km (Fig. 15). A propagated error of up to 0.006 ppbv is found over the altitude range of 15–35 km, where the largest value is located at the altitude of 21 km (56 %). Below the observer, the profile is saturated with a positive error, while depleted with a negative error. O_3 is not affected by the assumed errors on the pressure profile, the accuracy of the pressure profile is therefore of importance to retrieval of OH and other weak molecules.

For analysis of the real measurements, the pressure profile can be taken from the ECMWF (European Centre for Medium-Range Weather Forecasts) data. Alternatively, atmospheric pressure can be calculated from the temperature profile via the hydrostatic equation.

Regarding other interfering gases, inaccurate a priori knowledge of HCl and HO_2 does not affect the OH retrieval.

4 Capability of multi-channel simultaneous retrieval

During the flight, TELIS can measure two of three channels simultaneously. It is tempting to consider improving the retrieval accuracy by the simultaneous processing of several windows. Multi-window retrieval is commonly used for instruments covering broad spectral bands, notably Fourier transform spectrometer, e.g. MIPAS (Fischer et al., 2008), whereas the synergistic analysis of spectra measured by different instruments is discussed in few papers only, e.g. IASI and GOME-2 (Landgraf and Hasekamp, 2007), or IASI and MIPAS (Ceccherini et al., 2010). Here a joint retrieval from far infrared and submillimeter observations offers a novel aspect (to our knowledge Aura/MLS does not exploit the GHz and THz channels simultaneously). We focus on a combination of the 1.8 THz and 480–650 GHz channels since both channels observe a number of common molecules, e.g. HCl, HOCl, HO_2, NO, O_3, H_2O and its isotopologues. In this study

GID
3, 251–303, 2013

we investigate the retrieval capability of HCl by multi-channel fitting. Note that these two channels are characterized by different spectral response functions.

Table 2 summarizes the main instrument and atmospheric parameters. TELIS can measure signals at different observing and tangent altitudes during the flight, a corresponding change of geometry with respect to Table 1 has been made. The synthetic measurement is simulated for two HCl microwindows observed with the LO frequency set to 1877.63 and 619.10 GHz as utilized during the previous flights. Random noise is superimposed onto the measurement for each channel with the estimated signal-to-noise ratio. In addition to the target molecule, H_2O, O_3, O_2, NO_2, ClO, and HOCl were taken as the interfering molecules.

The state vector is constructed from the VMR profiles of the main target HCl and one auxiliary molecule O_3, with the a priori error of 90 %. The retrieval grid is discretized in 1.5 km between 10 and 32.5 km which is equivalent to the tangent spacing, and the same spacing above 32.5 km as in Sect. 3.1. In this section, the regularization parameters are estimated by minimizing certain objective functions corresponding to the main component of the state vector, i.e. the reconstruction of HCl. All retrievals are performed with $\lambda_{HCl} = 1 \times 10^{-4}$ and $\lambda_{O_3} = 0$.

In Fig. 16a the averaging kernels for HCl retrieval using the multi-channel measurement are compared with those using only the single-channel measurement. The averaging kernels for the multi-channel case indicate an improved vertical resolution below 20.5 km where the averaging kernels obtained from the measurement in the THz channel are rather wide. On the other hand, the averaging kernels for the multi-channel case below 20.5 km imply that the GHz channel data provides a better resolution of the retrieval product also over this altitude range. Above 20.5 km the averaging kernels for the profile obtained from the multi-channel data are quite similar to those obtained from the THz channel measurement alone. A noticeable quality improvement in terms of the degree of freedom for signal is also obtained. By using both channels concurrently, the corresponding smoothing error (Fig. 16b) indicates that regularization results in less information loss below 22 km and the noise error below 19 km is decreased by about

GID
3, 251–303, 2013

a factor of 5, as compared to the results using the THz channel only. In this case, the relative retrieval error is therefore 5–10 % better over the altitude range of 10–20.5 km. For the retrieval using the THz channel only, the noise error dominates the retrieval error over the whole altitude range due to the worse signal-noise-ratio, whereas the noise error is very closed to zero for the retrieval with the GHz channel data. The smoothing error for all retrievals is large below 20.5 km and the regularization can have an effect on the retrieval quality of HCl. By comparison with the results using the GHz channel alone, a smaller smoothing error given by the multi-channel measurement is achieved, although a slightly worse retrieval error is found above 20.5 km due to larger measurement noise in the THz channel. According to these results, the sensitivity of HCl in the THz channel microwindow is superior to that in the GHz channel microwindow at higher altitudes, while at lower altitudes the GHz channel data delivers a stronger HCl signal.

In Fig. 17 the errors of HCl with respect to the true profile for the three cases are depicted. The error for the multi-channel measurement is overall better than that retrieved from the THz channel measurement. A large improvement can be found below 17.5 km with respect to that using the GHz channel only. The largest error appears around 20.5 km where the noise error (see Fig. 16b) is largest below the observer in the THz channel measurement.

These results indicate that the multi-channel simultaneous retrieval can help to improve the quality of the retrieval by significantly better exploitation of information from the observations. Furthermore, the multi-channel fitting requires less iteration steps than both single-channel cases.

5 Conclusions

We have presented the retrieval code PILS for infrared/microwave limb sounding and applied it to the TELIS level-2 data processing. Compared to most stochastic data models used in the literature, our data analysis operates in a semi-stochastic setting. The forward model is based on an optimized line-by-line code, coupled with automatic

GID
3, 251–303, 2013

differentiation for evaluating Jacobians accurately and efficiently, and the inversion employs nonlinear least squares fitting with direct and iterative multi-parameter regularization methods.

A sensitivity study of hydroxyl radical (OH) retrieval from spectra recorded by the TELIS 1.8 THz channel has been given, assuming a single limb scan with a worst case signal-noise-ratio, but otherwise perfect instrumental knowledge. Both single- and multi-profile retrieval frameworks perform in decent quality. The results illustrate that OH can be derived from the TELIS observations in the lower and middle stratosphere. The relative retrieval error is typically 25 % at the lowest altitude due to the a priori knowledge and gradually improves with increasing altitude where the retrieval error is dominated by the noise error.

Furthermore, a sensitivity analysis on potential error sources has been conducted. We have simulated the calibration procedure in the forward model and retrieved OH from the calibrated measurements distorted by nonlinearity. The calibration error, mainly the nonlinearity effect, does not introduce a severe error on the OH retrieval.

However, the inaccurate knowledge of the receiver sideband ratio is estimated to induce an error in the retrieval, because the strong OH line lies in the upper sideband in the selected frequency microwindow. The results are found to be more severely influenced by larger biases. In particular, the pointing error could be another major error source for the OH retrieval.

The propagated errors due to the atmospheric profiles have also been investigated. The OH retrieval is very sensitive to the errors in the temperature and pressure profiles at lower altitudes where the concentration is rather low.

Besides, the capability of multi-channel simultaneous retrieval of hydrogen chloride (HCl) from the far infrared and submillimeter observations has been studied. The errors and averaging kernels demonstrate the improvement on the retrieval quality, particularly over the lower altitude range.

There are some important issues to be resolved, such as pointing retrieval, reliable temperature profile, and errors in spectroscopic parameters and continuum model. Our

GID
3, 251–303, 2013

current/future work focuses on analysis of the real measurement data from the three Kiruna campaigns, and we begin with the O_3 retrieval (see Kasai et al., 2013).

Acknowledgements. The authors would like to thank M. Birk and G. Wagner from DLR, A. de Lange and J. Landgraf from SRON for fruitful discussions on the TELIS measurement and its relevance to atmospheric research. Financial support for JX by the German Academic Exchange Service (DAAD) is appreciated.

The service charges for this open access publication have been covered by a Research Centre of the Helmholtz Association.

References

Anderson, G., Clough, S., Kneizys, F., Chetwynd, J., and Shettle, E.: AFGL atmospheric constituent profiles (0–120 km), Tech. Rep. TR-86-0110, AFGL, 1986. 263

Bakushinskii, A.: The problem of the convergence of the iteratively regularized Gauss–Newton method, Comput. Math. Phys., 32, 1353–1359, 1992. 259

Baron, P., Urban, J., Sagawa, H., Möller, J., Murtagh, D. P., Mendrok, J., Dupuy, E., Sato, T. O., Ochiai, S., Suzuki, K., Manabe, T., Nishibori, T., Kikuchi, K., Sato, R., Takayanagi, M., Murayama, Y., Shiotani, M., and Kasai, Y.: The Level 2 research product algorithms for the Superconducting Submillimeter-Wave Limb-Emission Sounder (SMILES), Atmos. Meas. Tech., 4, 2105–2124, doi:10.5194/amt-4-2105-2011, 2011. 268

Birk, M., Wagner, G., de Lange, G., de Lange, A., Ellison, B. N., Harman, M. R., Murk, A., Oelhaf, H., Maucher, G., and Sartorius, C.: TELIS: TErahertz and subMMW LImb Sounder – Project Summary After First Sucessful Flight, in: Proceedings of 21st International Symposium on Space Terahertz Technology, University of Oxford and STFC Rutherford Appleton Laboratory, 195–200, 2010. 263

Bischof, C., Carle, A., Hovland, P., Khademi, P., and Mauer, A.: ADIFOR 2.0 User's Guide (Revision D), Tech. Rep. ANL/MCS-TM-192, Argonne National Laboratory – Mathematics and Computer Science Division, 1998. 261

Bischof, C. H. and Bücker, H. M.: Computing Derivatives of Computer Programs, in: Modern Methods and Algorithms of Quantum Chemistry: Proceedings, edited by: Grotendorst, J.,

GID

3, 251–303, 2013

2nd Edn., NIC Series, Vol. 3, John von Neumann Institute for Computing, Jülich, 315–327, 2000. 262

Carli, B., Carlotti, M., Dinelli, B., Mencaraglia, F., and Park, J.: The mixing ratio of stratospheric hydroxyl radical from far infrared emission measurements, J. Geophys. Res., 94, 11049–11058, doi:10.1029/JD094iD08p11049, 1989. 254

Carlotti, M.: Global-fit approach to the analysis of limb–scanning atmospheric measurements, Appl. Opt., 27, 3250–3254, doi:10.1364/AO.27.003250, 1988. 257

Carlotti, M., Ade, P., Carli, B., Chipperfield, M., Hamilton, P., Mencaraglia, F., Nolt, I., and Ridolfi, M.: Diurnal variability and night detection of stratospheric hydroxyl radical from far infrared emission measurements, J. Atmos. Sol.-Terr. Phys., 63, 1509–1518, doi:10.1016/S1364-6826(01)00030-X, 2001. 254

Ceccherini, S., Carli, B., Cortesi, U., Bianco, S. D., and Raspollini, P.: Retrieval of the vertical column of an atmospheric constituent from data fusion of remote sensing measurements, J. Quant. Spectrosc. Ra., 111, 507–514, doi:10.1016/j.jqsrt.2009.09.001, 2010. 275

Clough, S., Kneizys, F., and Davies, R.: Line shape and the water vapor continuum, Atmos. Res., 23, 229–241, doi:10.1016/0169-8095(89)90020-3, 1989. 262

de Lange, A., Landgraf, J., and Hoogeveen, R.: Stratospheric isotopic water profiles from a single submillimeter limb scan by TELIS, Atmos. Meas. Tech., 2, 423–435, doi:10.5194/amt-2-423-2009, 2009. 255, 256, 268

de Lange, A., Birk, M., de Lange, G., Friedl-Vallon, F., Kiselev, O., Koshelets, V., Maucher, G., Oelhaf, H., Selig, A., Vogt, P., Wagner, G., and Landgraf, J.: HCl and ClO in activated Arctic air; first retrieved vertical profiles from TELIS submillimetre limb spectra, Atmos. Meas. Tech., 5, 487–500, doi:10.5194/amt-5-487-2012, 2012. 268

de Lange, G., Birk, M., Boersma, D., Derckson, J., Dmitriev, P., Ermakov, A., Filippenko, L., Golstein, H., Hoogeveen, R., de Jong, L., Khudchenko, A., Kinev, N., Kiselev, O., van Kuik, B., de Lange, A., van Rantwijk, J., Selig, A., Sobolev, A., Torgashin, M., de Vries, E., Wagner, G., Yagoubov, P., and Koshelets, V.: Development and characterization of the superconducting integrated receiver channel of the TELIS atmospheric sounder, Supercond. Sci. Technol., 23, 045016, doi:10.1088/0953-2048/23/4/045016, 2010. 253

Dennis Jr., J., Gay, D., and Welsch, R.: An adaptive nonlinear least–squares algorithm, ACM Trans. Math. Soft., 7, 348–368, doi:10.1145/355958.355965, 1981. 262

GID
3, 251–303, 2013

Doicu, A., Trautmann, T., and Schreier, F.: Numerical Regularization for Atmospheric Inverse Problems, Springer and Praxis Publishing, Berlin Heidelberg, XIII, 1–426, doi:10.1007/978-3-642-05439-6, 2010. 258, 259

Englert, C., Schimpf, B., Birk, M., Schreier, F., Krocka, M., Nitsche, R., Titz, R., and Summers, M.: The 2.5 THz heterodyne spectrometer THOMAS: Measurement of OH in the middle atmosphere and comparison with photochemical model results, J. Geophys. Res., 105, 22211–22223, doi:10.1029/2000JD900305, 2000. 255

Fischer, H., Birk, M., Blom, C., Carli, B., Carlotti, M., von Clarmann, T., Delbouille, L., Dudhia, A., Ehhalt, D., Endemann, M., Flaud, J. M., Gessner, R., Kleinert, A., Koopman, R., Langen, J., López-Puertas, M., Mosner, P., Nett, H., Oelhaf, H., Perron, G., Remedios, J., Ridolfi, M., Stiller, G., and Zander, R.: MIPAS: an instrument for atmospheric and climate research, Atm. Chem. Phys., 8, 2151–2188, doi:10.5194/acp-8-2151-2008, 2008. 275

Fox, P., Hall, A., and Schryer, N.: The PORT Mathematical Subroutine Library, ACM Trans. Math. Soft., 4, 104–126, doi:10.1145/355780.355789, 1978. 262

Friedl-Vallon, F., Maucher, G., Seefeldner, M., Trieschmann, O., Kleinert, A., Lengel, A., Keim, C., Oelhaf, H., and Fischer, H.: Design and characterization of the balloon-borne Michelson Interferometer for Passive Atmospheric Sounding (MIPAS-B2), Appl. Opt., 43, 3335–3355, doi:10.1364/AO.43.003335, 2004. 253, 273

Griewank, A.: Evaluating Derivatives: Principles and Techniques of Algorithmic Differentiation, SIAM, Philadelphia, PA, 2000. 261

Hascoët, L. and Pascual, V.: The Tapenade automatic differentiation tool: Principles, model, and specification, ACM Trans. Math. Soft., 39, 3, doi:10.1145/2450153.2450158, 2013. 261

Hedelt, P., Alonso, R., Brown, T., Collados Vera, M., Rauer, H., Schleicher, H., Schmidt, W., Schreier, F., and Titz, R.: Venus transit 2004: Illustrating the capability of exoplanet transmission spectroscopy, A & A, 533, A136, doi:10.1051/0004-6361/201016237, 2011. 261

Jucks, K., Johnson, D., Chance, K., Traub, W., Margitan, J., Osterman, G., Salawitch, R., and Sasano, Y.: Observations of OH, HO_2, H_2O, and O_3 in the upper stratosphere: Implications for HO_x photochemistry, Geophys. Res. Lett., 25, 3935–3938, doi:10.1029/1998GL900009, 1998. 254

Kasai, Y., Sagawa, H., Kreyling, D., Suzuki, K., Dupuy, E., Sato, T. O., Mendrok, J., Baron, P., Nishibori, T., Mizobuchi, S., Kikuchi, K., Manabe, T., Ozeki, H., Sugita, T., Fujiwara, M., Irimajiri, Y., Walker, K. A., Bernath, P. F., Boone, C., Stiller, G., von Clarmann, T., Orphal, J., Urban, J., Murtagh, D., Llewellyn, E. J., Degenstein, D., Bourassa, A. E., Lloyd, N. D., Froidevaux,

GID
3, 251–303, 2013

L., Birk, M., Wagner, G., Schreier, F., Xu, J., Vogt, P., Trautmann, T., and Yasui, M.: Validation of stratospheric and mesospheric ozone observed by SMILES from International Space Station, Atmos. Meas. Tech. Discuss., 6, 2643–2720, doi:10.5194/amtd-6-2643-2013, 2013. 279

Kikuchi, K., Nishibori, T., Ochiai, S., Ozeki, H., Irimajiri, Y., Kasai, Y., Koike, M., Manabe, T., Mizukoshi, K., Murayama, Y., Nagahama, T., Sano, T., Sato, R., Seta, M., Takahashi, C., Takayanagi, M., Masuko, H., Inatani, J., Suzuki, M., and Shiotani, M.: Overview and early results of the Superconducting Submillimeter-Wave Limb-Emission Sounder (SMILES), J. Geophys. Res., 115, D23306, doi:10.1029/2010JD014379, 2010. 253

Landgraf, J. and Hasekamp, O. P.: Retrieval of tropospheric ozone: The synergistic use of thermal infrared emission and ultraviolet reflectivity measurements from space, J. Geophys. Res., 112, D08310, doi:10.1029/2006JD008097, 2007. 275

Liou, K.-N.: An Introduction to Atmospheric Radiation, Academic Press, 2nd Edn., 2002. 256

Mair, U., Krocka, M., Wagner, G., Birk, M., Hübers, H.-W., Richter, H., Semenov, A., Hoogeveen, R., de Graauw, T., Yagoubov, P., Maurellis, A., Selig, A., Koshelets, V., Shitov, S., Goltsman, G., Voronov, B., Ellison, B., Kerridge, B., Matheson, D., Siddans, R., and Reburn, J.: TELIS – Development of a New Balloon Borne THz/Submm Heterodyne Limb Sounder, in: Proceedings of the 14. International Symposium on Space Terahertz Technology, Tucson, AZ, USA, April 2003, 204–214, 2004. 255

Melsheimer, C., Verdes, C., Bühler, S., Emde, C., Eriksson, P., Feist, D., Ichizawa, S., John, V., Kasai, Y., Kopp, G., Koulev, N., Kuhn, T., Lemke, O., Ochiai, S., Schreier, F., Sreerekha, T., Suzuki, M., Takahashi, C., Tsujimaru, S., and Urban, J.: Intercomparison of general purpose clear sky atmospheric radiative transfer models for the millimeter/submillimeter spectral range, Radio Sci., 40, RS1007, doi:10.1029/2004RS003110, 2005. 261

Mendrok, J., Schreier, F., and Höpfner, M.: Estimating cirrus cloud properties from MIPAS data, Geophys. Res. Lett., 34, L08807, doi:10.1029/2006GL028246, 2007. 261

Minschwaner, K., Manney, G. L., Wang, S. H., and Harwood, R. S.: Hydroxyl in the stratosphere and mesosphere – Part 1: Diurnal variability, Atmos. Chem. Phys., 11, 955–962, doi:10.5194/acp-11-955-2011, 2011. 255

Murtagh, D., Frisk, U., Merino, F., Ridal, M., Jonsson, A., Stegman, J., Witt, G., Eriksson, P., Jiménez, C., Megie, G., de la Noë, J., Ricaud, P., Baron, P., Pardo, J. R., Hauchcorne, A., Llewellyn, E. J., Degenstein, D. A., Gattinger, R. L., Lloyd, N. D., Evans, W. F., McDade, I. C., Haley, C. S., Sioris, C., von Savigny, C., Solheim, B. H., McConnell, J. C., Strong,

GID
3, 251–303, 2013

K., Richardson, E. H., Leppelmeier, G. W., Kyrölä, E., Auvinen, H., and Oikarinen, L.: An overview of the Odin atmospheric mission, Can. J. Phys., 80, 309–319, doi:10.1139/p01-157, 2002. 252

Pickett, H. and Peterson, D.: Stratospheric OH Measurements with a far-infrared limb observing spectrometer, J. Geophys. Res., 98, 20507–20515, 1993. 254

Rodgers, C.: Inverse Methods for Atmospheric Sounding: Theory and Practise, World Scientific, Singapore, 2000. 258

Rothman, L., Gordon, I., Barbe, A., Benner, D. C., Bernath, P., Birk, M., Boudon, V., Brown, L., Campargue, A., Champion, J.-P., Chance, K., Coudert, L., Dana, V., Devi, V., Fally, S., Flaud, J.-M., Gamache, R., Goldman, A., Jacquemart, D., Kleiner, I., Lacome, N., Lafferty, W., Mandin, J.-Y., Massie, S., Mikhailenko, S., Miller, C., Moazzen-Ahmadi, N., Naumenko, O., Nikitin, A., Orphal, J., Perevalov, V., Perrin, A., Predoi-Cross, A., Rinsland, C., Rotger, M., Simecková, M., Smith, M., Sung, K., Tashkun, S., Tennyson, J., Toth, R., Vandaele, A., and Auwera, J. V.: The HITRAN 2008 molecular spectroscopic database, J. Quant. Spectrosc. Ra., 110, 533–572, doi:10.1016/j.jqsrt.2009.02.013, 2009. 262

Schreier, F.: Optimized evaluation of a large sum of functions using a three-grid approach, Comp. Phys. Comm., 174, 783–802, doi:10.1016/j.cpc.2005.12.015, 2006. 261

Schreier, F.: Optimized implementations of rational approximations for the Voigt and complex error function, J. Quant. Spectrosc. Ra., 112, 1010–1025, doi:10.1016/j.jqsrt.2010.12.010, 2011. 261

Schreier, F. and Böttger, U.: MIRART, A line-by-line code for infrared atmospheric radiation computations incl. derivatives, Atmos. Ocean. Opt., 16, 262–268, 2003. 261

Schreier, F. and Schimpf, B.: A New Efficient Line-By-Line Code for High Resolution Atmospheric Radiation Computations incl. Derivatives, in: IRS 2000: Current Problems in Atmospheric Radiation, edited by: Smith, W. and Timofeyev, Y., A. Deepak Publishing, 381–384, 2001. 261

Suttiwong, N.: Development and characteristics of the balloon borne instrument TELIS (TEhertz and submillimeter LImb Sounder): 1.8 THz receiver, Ph.D. Thesis, University of Bremen, 2010. 254, 257

Suttiwong, N., Birk, M., Wagner, G., Krocka, M., Wittkamp, M., Haschberger, P., Vogt, P., and Geiger, F.: Development and characterization of the balloon borne instrument TELIS (TEhertz and Submm LImb Sounder): 1.8 THz receiver, in: Proc. 19th ESA Symposium on

GID
3, 251–303, 2013

European Rocket and Balloon Programmes and Related Research, Bad Reichenhall, Germany, 2009. 253

Tikhonov, A.: On the Solution of Incorrectly Stated Problems and a Method of Regularization, Dokl. Acad. Nauk SSSR, 151, 501–504, 1963. 257

Ungermann, J., Blank, J., Lotz, J., Leppkes, K., Hoffmann, L., Guggenmoser, T., Kaufmann, M., Preusse, P., Naumann, U., and Riese, M.: A 3-D tomographic retrieval approach with advection compensation for the air-borne limb-imager GLORIA, Atmos. Meas. Tech., 4, 2509–2529, doi:10.5194/amt-4-2509-2011, 2011. 261

Urban, J., Lautié, N., Flochmoën, E. L., Jiménez, C., Eriksson, P., Dupuy, E., Amraoui, L. E., Ekström, M., Frisk, U., Murtagh, D., de La Noë, J., Olberg, M., and Ricaud, P.: Odin/SMR limb observations of stratospheric trace gases: Level 2 processing of ClO, N_2O, O_3, and HNO_3, J. Geophys. Res., 110, D14, doi:10.1029/2004JD005741, 2005. 268

Vasquez, M., Gottwald, M., Gimeno García, S., Krieg, E., Lichtenberg, G., Slijkhuis, S., Schreier, F., Snel, R., and Trautmann, T.: Venus observations from ENVISAT–SCIAMACHY: Measurements and modeling, Adv. Space Res., 51, 835–848, doi:10.1016/j.asr.2012.09.046, 2013. 261

von Clarmann, T., Höpfner, M., Funke, B., López-Puertas, M., Dudhia, A., Jay, V., Schreier, F., Ridolfi, M., Ceccherini, S., Kerridge, B., Reburn, J., and Siddans, R.: Modeling of atmospheric mid-infrared radiative transfer: the AMIL2DA algorithm intercomparison experiment, J. Quant. Spectrosc. Ra., 78, 381–407, doi:10.1016/S0022-4073(02)00262-5, 2002. 261

Waters, J., Froidevaux, L., Harwood, R., Jarnot, R., Pickett, H., Read, W., Siegel, P., Cofield, R., Filipiak, M., Flower, D., Holden, J., Lau, G., Livesey, N., Manney, G., Pumphrey, H., Santee, M., Wu, D., Cuddy, D., Lay, R., Loo, M., Perun, V., Schwartz, M., Stek, P., Thurstans, R., Boyles, M., Chandra, K., Chavez, M., Chen, G.-S., Chudasama, B., Dodge, R., Fuller, R., Girard, M., Jiang, J., Jiang, Y., Knosp, B., LaBelle, R., Lam, J., Lee, K., Miller, D., Oswald, J., Patel, N., Pukala, D., Quintero, O., Scaff, D., Van Snyder, W., Tope, M., Wagner, P., and Walch, M.: The Earth observing system microwave limb sounder (EOS MLS) on the Aura Satellite, IEEE Trans. Geosci. Remote Sens., 44, 1075–1092, doi:10.1109/TGRS.2006.873771, 2006. 253

Zdunkowski, W., Trautmann, T., and Bott, A.: Radiation in the Atmosphere – A Course in Theoretical Meteorology, Cambridge University Press, 2007. 256

GID

3, 251–303, 2013

Table 1. Major instrument and geometry parameters used for simulating the synthetic spectra observed for the OH microwindow. The channel notation THz stands for the 1.8 THz channel.

Parameter	Description
Channel	THz
LO frequency	1830.10 GHz
Intermediate frequency	4–6 GHz
Spectral resolution	2.16 MHz
ILS function	Hamming apodization
Field-of-view (FWHM)	Gaussian (6.3 arcmin)
Sideband ratio	1.0
Signal-to-noise ratio	35
Top-of-atmosphere	85 km
Observing altitude	35 km
Tangent altitudes	15–33 km
Vertical sampling	2 km

GID
3, 251–303, 2013

Table 2. Major instrument and geometry settings for multi-channel retrieval simulation. The channel notation GHz stands for the 480–650 GHz channel.

Parameter	Description	
Channel	THz	GHz
LO frequency	1877.63 GHz	619.10 GHz
Intermediate frequency	4–6 GHz	5–7 GHz
ILS function	Hamming apodization	Lorentzian
Field-of-view (FWHM)	Gaussian (6.3 arcmin)	Gaussian (10.8 arcmin)
Signal-to-noise ratio	30	110
Top-of-atmosphere	85 km	
Observing altitude	34 km	
Tangent altitudes	10–32.5 km	
Vertical sampling	1.5 km	

GID
3, 251–303, 2013

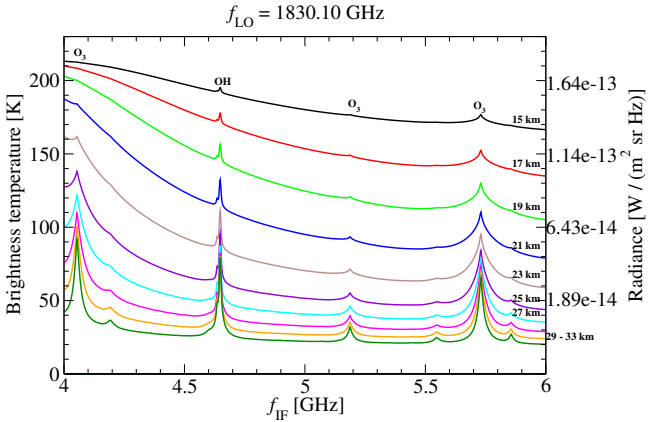

Fig. 1. Noise-free spectra (radiance and equivalent brightness temperature) simulated for a local oscillator frequency f_{LO} = 1830.10 GHz with an intermediate frequency range of 4–6 GHz, recording in double sideband mode with a sideband ratio of 1.0. The flight altitude is 35 km and the tangent altitudes are given to the right of the panel.

GID
3, 251–303, 2013

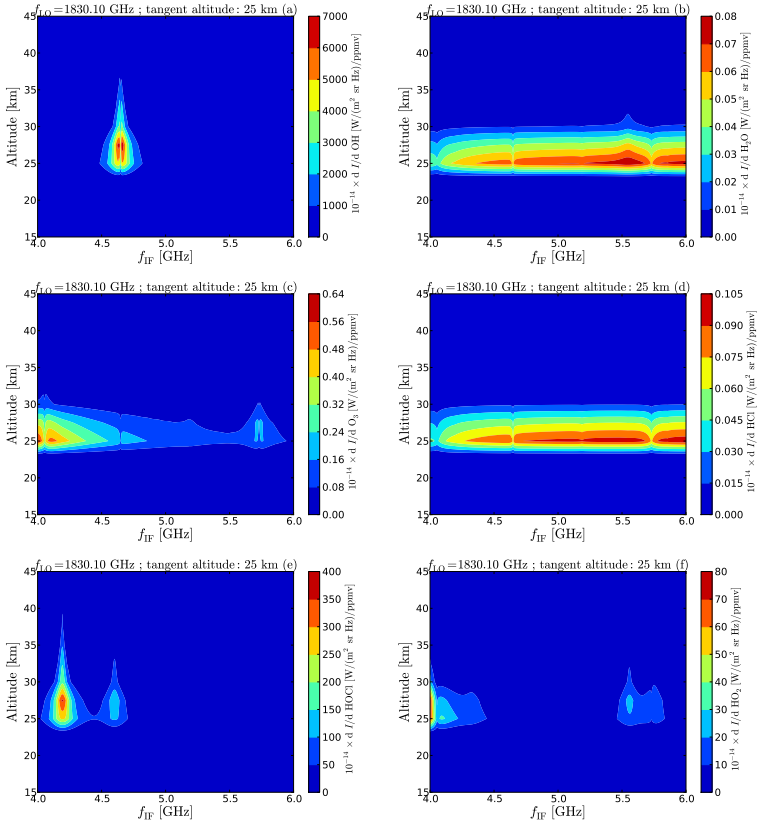

Fig. 2. Jacobian for molecular concentration profiles evaluated at an altitude grid between 15 and 45 km for a tangent altitude of 25 km. The molecules are OH **(a)**, H_2O **(b)**, O_3 **(c)**, HCl **(d)**, HOCl **(e)**, and HO_2 **(f)**.

GID
3, 251–303, 2013

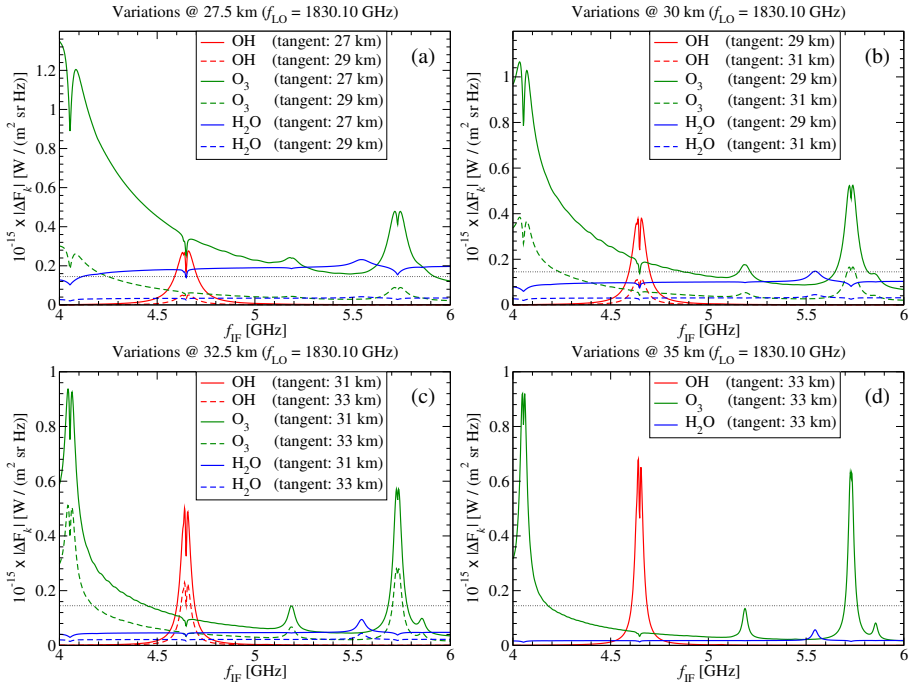

Fig. 3. Sensitivity study: variations of the limb radiances for a 10 % variation of the concentration profiles of OH, O_3, and H_2O at the altitude levels of 27.5 **(a)**, 30 **(b)**, 32.5 **(c)**, and 35 km **(d)**. The dotted horizontal lines delimit the noise domain.

GID
3, 251–303, 2013

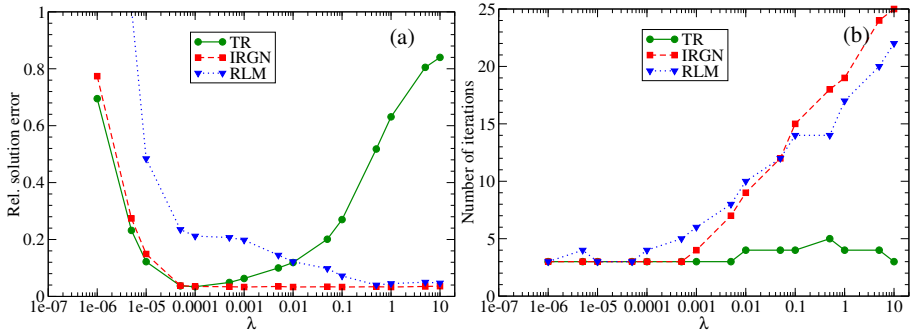

Fig. 4. Relative solution errors **(a)** and the number of iteration steps **(b)** for different values of the regularization parameter. The results are for one-profile retrieval of OH and correspond to Tikhonov regularization (TR), the iteratively regularized Gauss–Newton (IRGN) method, and the regularizing Levenberg–Marquardt (RLM) method.

GID
3, 251–303, 2013

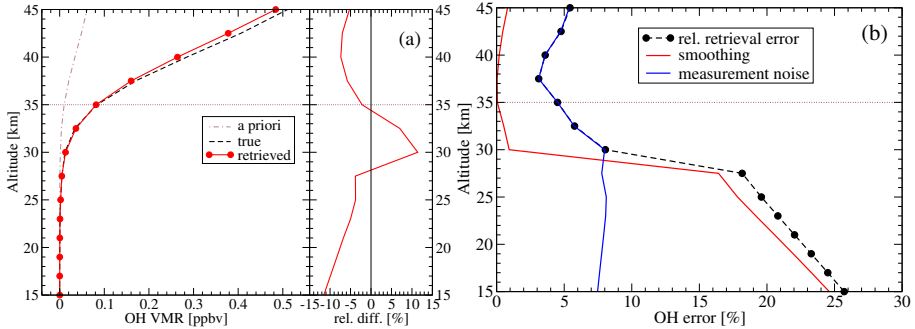

Fig. 5. Results of single OH retrieval and corresponding diagnostic quantities as a function of altitude. **(a)**: retrieved VMR profile and corresponding errors in terms of relative difference with respect to the true profile. The dashed black line refers to the true profile. **(b)**: corresponding properties of the retrieval, i.e. relative retrieval error, smoothing and noise errors.

GID
3, 251–303, 2013

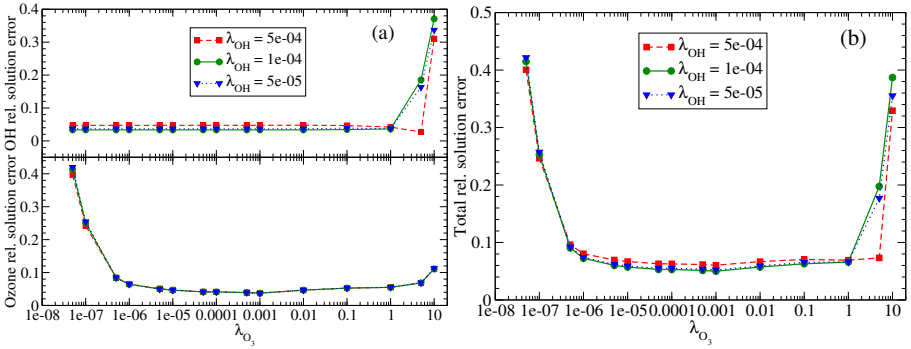

Fig. 6. Determination of the regularization parameters for two-profile retrieval of OH and O_3. **(a)**: relative solution errors of OH and O_3 versus different regularization parameters of OH and O_3. **(b)**: total solution errors versus the regularization parameters of OH and O_3.

GID
3, 251–303, 2013

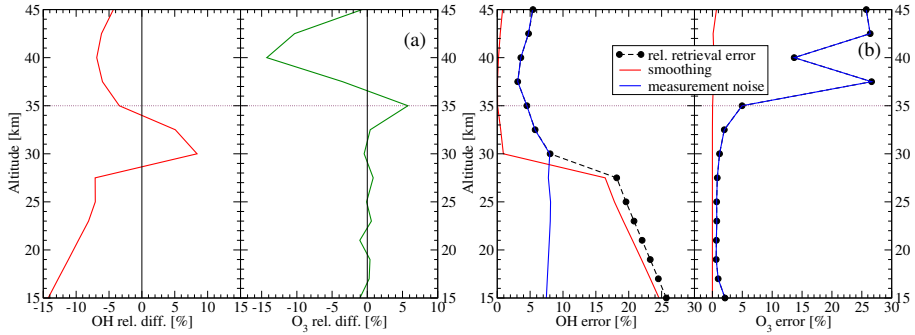

Fig. 7. Retrieval results for two-profile retrieval as a function of altitude. **(a)**: relative differences for joint retrieval of OH and O_3. **(b)**: relative retrieval error, smoothing and noise errors for joint retrieval of OH and O_3.

GID
3, 251–303, 2013

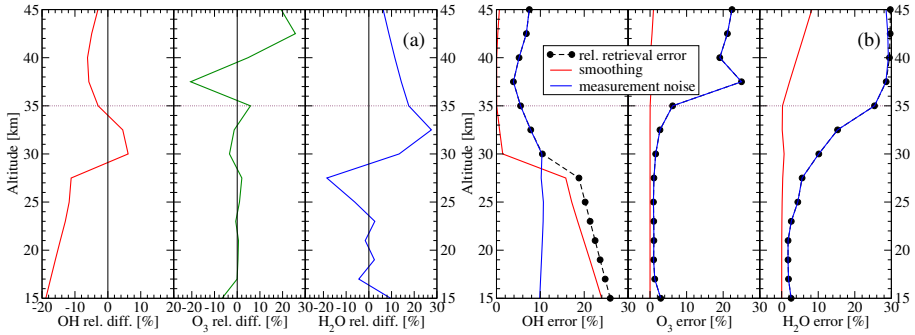

Fig. 8. Retrieval results for three-profile retrieval as a function of altitude. **(a)**: relative differences for joint retrieval of OH, O_3, and H_2O. **(b)**: relative retrieval error, smoothing and noise errors for joint retrieval of OH, O_3, and H_2O.

GID
3, 251–303, 2013

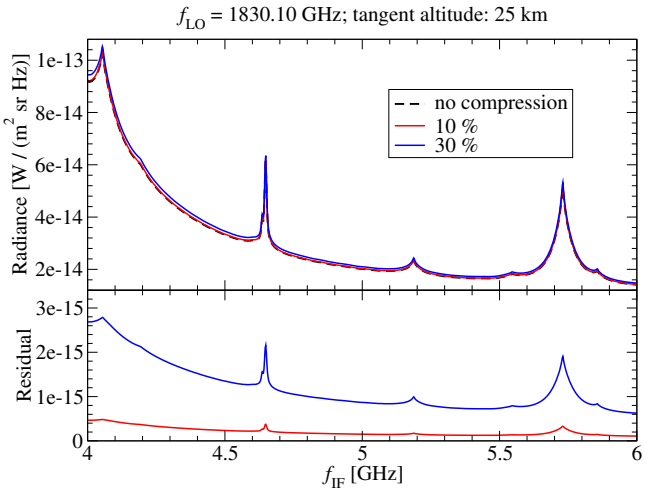

Fig. 9. Modelled calibrated spectrum measured at the tangent altitude of 25 km and corresponding residuals with respect to the pure model spectrum. The assumed compressions of 10 and 30 % in the hot load measurement are taken into account.

GID
3, 251–303, 2013

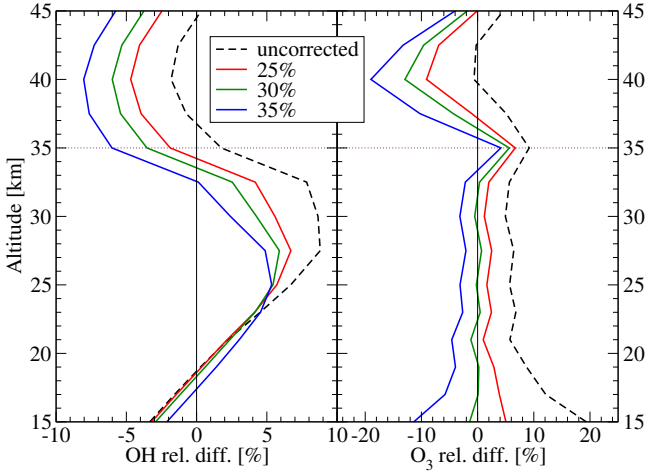

Fig. 10. Relative difference of OH and O_3. The retrievals are done for the noisy synthetic measurements that are generated by the calibrated spectra with the compression of 30 % in the hot load. 5 % uncertainty is taken into account in the pseudo-correction procedure: the compression is set to 25 and 35 % for two repeated retrievals.

GID
3, 251–303, 2013

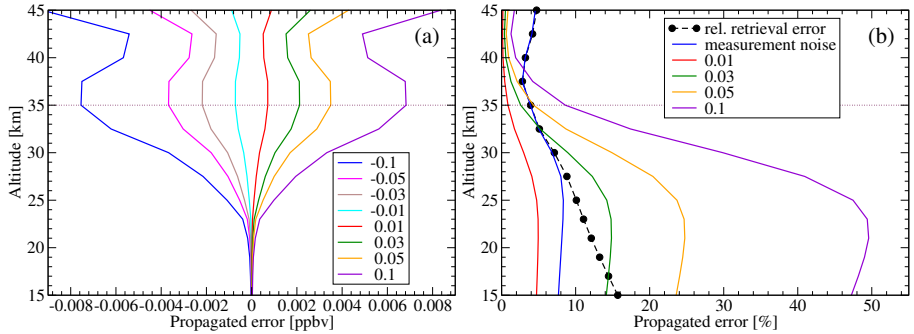

Fig. 11. Propagated error of sideband ratio onto the OH retrieval with the sideband ratio bias η. **(a)**: results in terms of absolute unit (VMR) with respect to the values ±0.01, ±0.03, ±0.05, and ±0.1 for η. **(b)**: results in terms of relative unit in percent of the true profile with respect to the positive values for η. For reference the retrieval error and the noise error caused by the measurement noise are included in this plot.

GID
3, 251–303, 2013

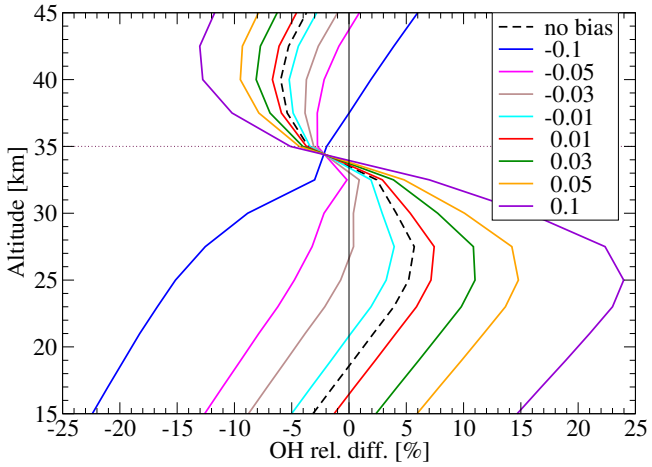

Fig. 12. Errors for OH retrieval in terms of relative difference with different values of relative bias η in the sideband ratio. The retrievals are performed using the synthetic measurement for ideal sideband ratio $r = 1.0$. For reference the retrieval result for the assumed sideband ratio $r = 1.0$ is given in dashed black line.

GID
3, 251–303, 2013

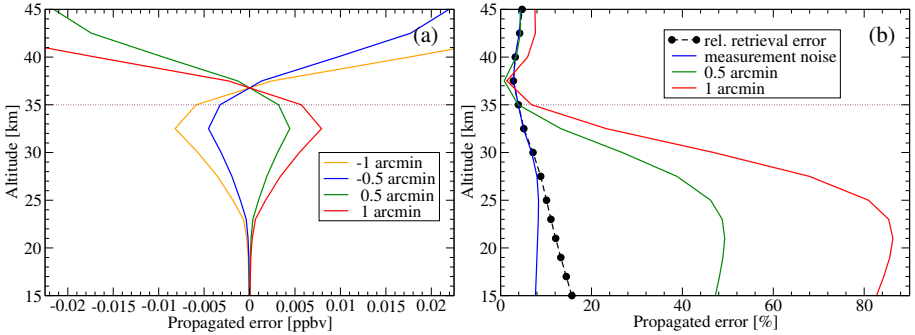

Fig. 13. Propagated error of pointing onto the OH retrieval with the error on the systematic pointing bias. By assuming ±0.5 and ±1 arcmin, respectively, the results in terms of absolute unit **(a)** and relative unit **(b)** with respect to the true profile are shown.

GID
3, 251–303, 2013

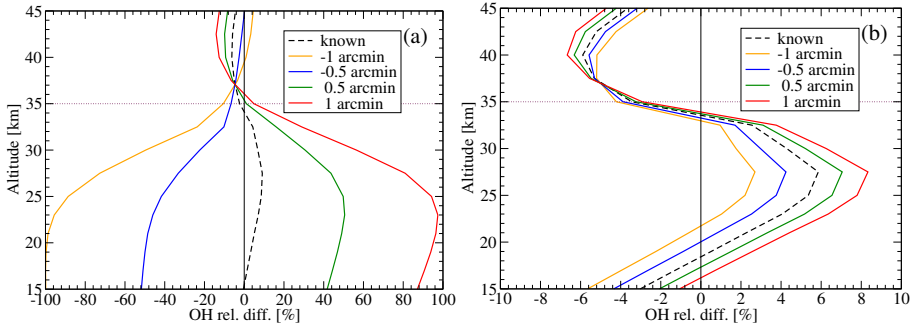

Fig. 14. Relative differences in the OH profile for single-target retrieval **(a)** and joint retrieval of OH and O_3 **(b)** with uncertainties of 0.5 and 1 arcmin in the systematic pointing bias. For reference the retrieval result for the perfectly known pointing information is given in dashed black line.

GID
3, 251–303, 2013

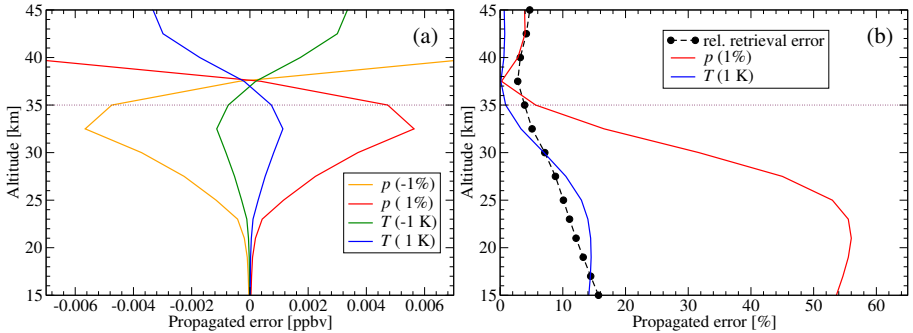

Fig. 15. Propagated errors of atmospheric profiles onto the OH retrieval. By assuming errors of −1 and 1 K in the temperature profile and errors of −1 and 1 % in the pressure profile, respectively, the results in terms of absolute unit **(a)** and relative unit **(b)** with respect to the true profile are shown. The black dashed line refers to the retrieval error in case of the exact temperature profile.

GID
3, 251–303, 2013

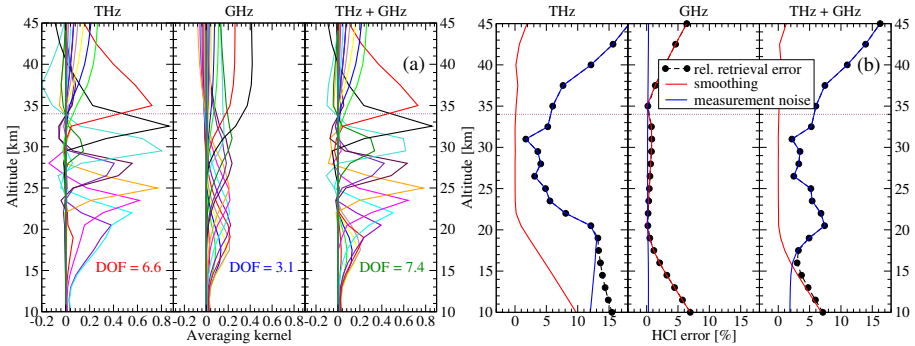

Fig. 16. (a): averaging kernels for HCl retrieval using the single-channel measurement in the 1.8 THz and 480–650 GHz channels, and the multi-channel measurement in both channels. The notation DOF stands for the degree of freedom for signal. **(b)**: relative retrieval error, smoothing and noise errors of HCl for the single- and multi-channel fitting.

GID
3, 251–303, 2013

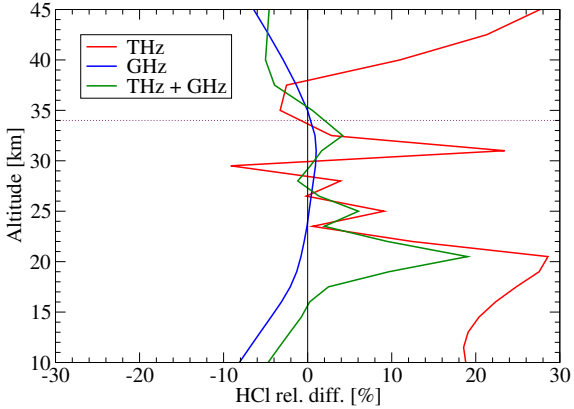

Fig. 17. Relative differences of HCl for the single- and multi-channel retrievals. The retrievals are done with the THz, GHz, and the combination of THz and GHz data, respectively.

GID
3, 251–303, 2013